Theoretical study of pattern formation during the catalytic oxidation of CO on Pt{100} at low pressures

Alexandra T. Anghel
Department of Applied Mathematics and Theoretical Physics, University of Cambridge, Wilberforce Road, Cambridge CB3 0WA, United Kingdom

Rebecca B. Hoyle[a)]
Department of Mathematics, University of Surrey, Guildford, Surrey GU2 7XH, United Kingdom

Isabel M. Irurzun
Facultad de Ciencias Exactas, INIFTA, Universidad Nacional de La Plata, 1900 La Plata, Argentina

Michael R. E. Proctor
Department of Applied Mathematics and Theoretical Physics, University of Cambridge, Wilberforce Road, Cambridge CB3 0WA, United Kingdom

David A. King
Department of Chemistry, University of Cambridge, Lensfield Road, Cambridge CB2 1EW, United Kingdom

(Received 25 May 2007; accepted 18 September 2007; published online 25 October 2007)

Theoretical studies have thus far been unable to model pattern formation during the reaction in this system on physically feasible length and time scales. In this paper, we derive a computational reaction-diffusion model for this system in which most of the input parameters have been determined experimentally. We model the surface on a mesoscopic scale intermediate between the microscopic size of CO islands and the macroscopic length scale of pattern formation. In agreement with experimental investigations [M. Eiswirth *et al.*, Z. Phys. Chem., Neue Folge **144**, 59 (1985)], the results from our model divide the CO and O_2 partial pressure parameter space into three regions defined by the level of CO coverage or the presence of sustained oscillations. We see CO fronts moving into oxygen-covered regions, with the 1×1 to hex phase change occurring at the leading edge. There are also traveling waves consisting of successive oxygen and CO fronts that move into areas of relatively high CO coverage, and in this case, the phase change is more gradual and of lower amplitude. The propagation speed of these reaction waves is similar to those observed experimentally for CO and oxygen fronts [H. H. Rotermund *et al.*, J. Chem. Phys. **91**, 4942 (1989); H. H. Rotermund *et al.*, Nature (London) **343**, 355 (1990); J. Lauterbach and H. H. Rotermund, Surf. Sci. **311**, 231 (1994)]. In the two-dimensional version of our model, the traveling waves take the form of target patterns emitted from surface inhomogeneities. © *2007 American Institute of Physics*. [DOI: 10.1063/1.2796174]

INTRODUCTION

A number of catalytic reactions exhibit complex dynamic behavior, including kinetic oscillations with both temporal and spatial characteristics. The oxidation of carbon monoxide on Pt{100}, which follows a Langmuir-Hinshelwood mechanism,[5] is a well researched process that falls in this category.[6]

The clean Pt{100} surface can be prepared in a metastable ideal bulk-terminated (1×1) structure at 300 K. On heating above 500 K the surface restructures to a more stable arrangement, in which the top layer adopts a quasihexagonal structure and the second layer retains the square array of the {100} surface. This phase is referred to as Pt{100}-hex.[7] The energy difference between the two clean solid surfaces has been measured calorimetrically and found to be 20 kJ/mol of surface platinum atoms (and equivalent to 0.21 eV per 1×1 area).[8] This procedure relies on the fact that adsorption of several gases can induce or lift the surface reconstruction, thereby allowing the construction of thermodynamic cycles that provide a direct measurement of the heat of reconstruction.

At surface temperatures above 380 K adsorption of CO on Pt{100}-hex leads to a lifting of the reconstruction.[9–11] The rate of transformation to the 1×1 phase follows a nonlinear growth power law in terms of the local coverage of CO on the hex phase, θ_{CO}^{hex}.[9–11] The rate of 1×1 island growth is given by $r_g(\theta)=k(\theta_{CO}^{hex})^{4.17}$, where k is the rate constant, and shows no dependence on substrate temperature. This strong nonlinearity results in a flux-dependent sticking probability for CO.[12] The growth rate was also shown to be independent of the exposure history and of the coverage of the 1×1 phase, $\theta_{1\times1}$.[10] Thiel *et al.*[13] have shown that the surface phase transformation leads to the formation of CO-dense islands on the 1×1 phase, with a CO coverage of about 0.5 ML (where 1 ML corresponds to the Pt atom den-

[a)]Electronic mail: r.hoyle@surrey.ac.uk

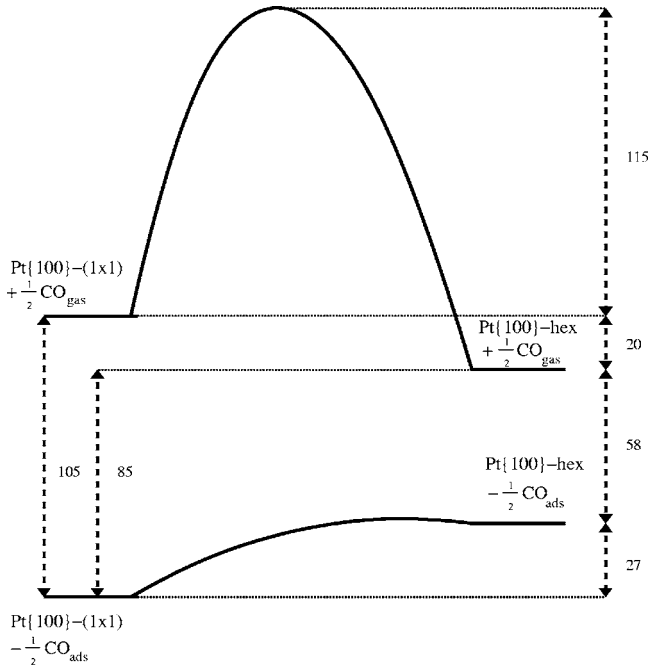

FIG. 1. Schematic energy level diagram for the CO-induced clean hex↔1×1 phase transition on Pt{100}. Following Yeo *et al.* (Ref. 8), all units are quoted in kJ/mol of surface platinum atoms.

sity in the ideal 1×1 surface). Since the nonlinear growth rate of the 1×1 phase is negligible at a very low coverage of CO on the Pt{100}-hex phase (i.e., $\theta_{\mathrm{CO}}^{\mathrm{hex}} \leqslant 0.02$ ML) and interactions between molecules can be ignored, the rate of desorption of CO from the hex phase was modeled by $r_d(\theta) = \nu \theta_{\mathrm{CO}}^{\mathrm{hex}} e^{-E/RT}$, where E is the desorption energy. Isothermal desorption measurements found $E = 105$ kJ/mol of CO, while $\nu = 3.7 \times 10^{12}$ s^{-1}.[14] The adsorption heat for CO on the 1×1 phase is much larger [$E = -225$ kJ/mol of CO (Ref. 13)], indicating that the difference in adsorption energetics is the driving force for the CO-induced lifting of the hex reconstruction. Furthermore, the energy gained in converting Pt{100}-hex with 0.5 ML of CO to Pt{100}-1×1 with 0.5 ML of CO is 27 kJ/mol of surface Pt atoms. Low energy electron diffraction (LEED) intensity measurements have determined the activation barrier for the conversion of the clean surface from 1×1 to hex to be 115 kJ/mol of surface platinum atoms.[13]

Following Yeo *et al.*,[8] we reproduce their schematic potential energy diagram (Fig. 1) relating the clean surface phases and the two CO-covered surface phases. The integral heats of adsorption shown here are 105 and 85 kJ/mol of surface platinum atoms for the 1×1 and hex surfaces, respectively. The activation barrier for diffusion/trapping of CO from the hex to the 1×1 phase is unknown but it is believed to be very small and taken as zero in our modeling since it proceeds even at 100 K. The activation energy for CO migration/untrapping from 1×1 to hex is, however, taken to be the difference between the CO desorption energies from each. We use the value $E = 154$ kJ/mol (at $\theta = 0$) adopted by Hopkinson and King[11] for the desorption energy from the 1×1 phase, and so the activation energy for CO untrapping is 49 kJ mol^{-1}.

We are going to concentrate now on modeling what is observed during the oxidation of CO on Pt{100}. In a recent letter,[15] we summarized numerical simulation results from the first faithful reaction-diffusion model to describe pattern formation in this system on experimentally realistic length and time scales. In this article, we focus on the derivation of the reaction-diffusion equations that define our model and present the results of numerical integrations and comparison with experiments in detail.

At pressures where global coupling of the surface through the gas phase is important the flux-dependent CO sticking probability maintains an in-phase behavior in the macroscopic properties across the whole crystal surface.[9–11] This manifests itself as regular and irregular self-maintaining oscillations of integral properties such as the rate of reaction and work function changes across the whole crystal surface.[1,16–18] However, in certain pressure regimes, spatial structure and self-organization have been observed by various surface imaging techniques to accompany the oscillations in the macroscopic reaction rate.[2–4,19] This typically takes the form of continuously varying patches of predominantly oxygen- and CO-covered surface whose arrangement changes in time through the passage of traveling reaction waves. These waves are of two types: relatively slow-moving CO fronts, at which the 1×1 to hex phase relaxation occurs, and faster oxygen fronts not accompanied by phase change.

To be able to build a macroscopic account of the spatiotemporal behavior of this reactive system, all the information available at the microscopic level is required. This includes the above description of adsorption of CO at the two clean phases of Pt{100}, information on the dissociative adsorption of O_2 at the surface and the other microscopic events that take place, as summarized by the following reaction scheme:

$$\mathrm{CO_{gas}} + \mathrm{Pt\{100\}hex} \overset{k_1,k_2}{\Leftrightarrow} \mathrm{CO_{hex}}, \tag{1}$$

$$\mathrm{CO_{gas}} + \mathrm{Pt\{100\}(1\times 1)} \overset{k_1,k_3}{\Leftrightarrow} \mathrm{CO_{1\times 1}}, \tag{2}$$

$$\mathrm{CO_{hex}} + \mathrm{Pt\{100\}(1\times 1)} \overset{k_4,k_5}{\Leftrightarrow} \mathrm{CO_{1\times 1}} + \mathrm{Pt\{100\}hex}, \tag{3}$$

$$\tfrac{1}{2}\mathrm{O_{2gas}} + \mathrm{Pt\{100\}(1\times 1)} \xrightarrow{k_6} \mathrm{O_{1\times 1}}, \tag{4}$$

$$n\mathrm{CO_{hex}} + m\mathrm{Pt\{100\}hex} \xrightarrow{k_8} n\mathrm{CO_{1\times 1}} + m\mathrm{Pt\{100\}(1\times 1)}, \tag{5}$$

$$\mathrm{Pt\{100\}(1\times 1)} \xrightarrow{k_9} \mathrm{Pt\{100\}hex}. \tag{6}$$

Finally, the reactive step is given by

$$\mathrm{CO_{1\times 1}} + \mathrm{O_{1\times 1}} \xrightarrow{k_7} \mathrm{CO_{2gas}} + 2\mathrm{Pt\{100\}(1\times 1)}, \tag{7}$$

where surface chemisorbed species are denoted by the subscripts hex and 1×1 and the gaseous species by gas.

The adsorption probability of O_2 on the Pt{100}-hex phase is less than 0.001 and is taken to be negligible in our

TABLE I. Experimental parameters for CO and O_2 adsorption on Pt{100}. Activation energies are labeled as E_a, while rate constants are labeled as k and sticking probabilities are denoted by S. Critical coverages for the adsorbate-induced phase transition are denoted by θ_{crit}.

Process	Parameter	E_a (kJ mol^{-1})	ν (s^{-1})
CO impingement rate	$k_1=2.22\times10^5$ ML mbar^{-1} s^{-1}		
O_2 impingement rate	$k_6=2.08\times10^5$ ML mbar^{-1} s^{-1}		
CO sticking on hex	$S_{CO}^{hex}=0.78$		
CO sticking on 1×1	$S_{CO}^{1\times1}=0.91(\theta=0)$		
O_2 sticking on 1×1	$S_{O_2}^{1\times1}=0.31(\theta=0)$		
CO desorption from hex	k_2	$E_2=105$	$\nu_2=3.7\times10^{12}$
CO desorption from 1×1	k_3	$E_3=154(\theta=0)$	$\nu_3=1.0\times10^{15}$
CO trapping	k_4	0	$\nu_5\nu_2S_{CO}^{1\times1}/\nu_3S_{CO}^{hex}$
CO untrapping	k_5	$E_3-E_2=49$	$\nu_5=1.0\times10^4$
$CO+O_2$ reaction	k_7	$E_7=58.6$	$\nu_7=2.0\times10^9$
CO (un)trapping	1×1 boundary length $B=1$		
	Phase-transition parameters		
hex$\rightarrow1\times1$	k_8	0	$\nu_8=4.9\times10^4$
hex$\rightarrow1\times1$	Reaction order $n=4.17$		
$1\times1\rightarrow$hex	k_9	108	$\nu_9=2.5\times10^{11}$
$1\times1\rightarrow$hex	$\theta_{crit}^{CO}=0.25$ ML		
$1\times1\rightarrow$hex	$\theta_{crit}^{O}=0.40$ ML		

model; while that on the 1×1 phase is significant and around 0.1.[20] Preadsorbed oxygen on 1×1 has no inhibiting effect on CO adsorption; however, the uptake of oxygen is inhibited by the presence of adsorbed CO.[16] In our model, both sticking probabilities are taken to depend on the total local adsorbate coverage, following Refs. 21 and 22, but this simplification is insignificant, as the local oxygen coverage is very low throughout. Desorption of CO takes place in the temperature range of interest (450–530 K), while oxygen desorption can be neglected under these conditions.[16]

The rates of migration of CO from the hex phase onto the 1×1 phase (trapping) and that of the reverse process (untrapping), both described by Eq. (3), depend on the relative length of the boundary between the hex and 1×1 areas, B. The parameter B has been modeled by fitting a set of differential equations describing the interaction of CO with both phases of Pt{100} and was found to be a constant, independent of coverage, for a wide range of CO fluxes.[11,12] In accordance with this model, we choose B to be 1. The constancy of B suggests a highly anisotropic 1×1 island growth,[11,12] which is supported by more recent scanning tunneling microscopy experiments by Borg *et al.*[23] who found much faster growth along the $[0\bar{1}1]$ direction than along the [011] direction at 300 K for an initial Pt{100}-hex surface rotated by 0.7°.

The growth of 1×1 islands does not occur by the accretion of individual CO molecules as they diffuse to the island boundaries:[9–11] instead, four CO molecules on the hex phase are involved in the concerted conversion of a patch of hex to 1×1 during the nucleation and growth of the 1×1 islands. Since the 1×1 phase forms as 0.5 ML dense CO islands, this implies that the *minimum* number of surface Pt atoms involved in surface restructuring is eight (i.e., $m\geqslant8$).

Data available from experimental studies and used in our model are shown in Table I. We use the same parameters as Gruyters *et al.*,[21] who, in turn, adopted many of them from Hopkinson and King.[11] The coverage-dependent sticking probabilities of CO and oxygen on the 1×1 phase are adapted from experimental data as in Ref. 24. We use the sticking probability of oxygen on "freed" sites, recently made available by CO desorption or CO_2 formation[21] for $S_{O_2}^{1\times1}$.

KINETIC RATE EQUATIONS

The kinetic rate equations describing the reaction scheme given in Eqs. (1)–(7) take standard chemical kinetic forms based on the model of Gruyters *et al.*,[21] except that we explicitly consider the fraction of sites available to adsorption, trapping, and untrapping processes, and that we ignore the distinction between free and freed sites as this does not seem to be important in our model. Furthermore, our revised model explicitly couples the phase transition with surface diffusion, thereby allowing the development of a spatially extended model, and takes into account the detailed experimental evidence regarding the reaction kinetics.

We write θ_{hex} and $\theta_{1\times1}$ for the coverages of hex and 1×1 phase, respectively (i.e., the fractions of the surface in each of these phases), and we, therefore, have $\theta_{hex}+\theta_{1\times1}=1$. We then write θ_{CO}^{hex}, $\theta_{CO}^{1\times1}$, and $\theta_{O}^{1\times1}$ for the *local* adsorbate coverages on the hex (i.e., θ_{hex}) and 1×1 (i.e., $\theta_{1\times1}$) phases. Finally, we denote by θ_e^{hex} and $\theta_e^{1\times1}$ the local coverages of empty sites on the hex and 1×1 phases, respectively, such that the local coverages satisfy

$$\theta_{CO}^{hex}+\theta_e^{hex}=1,$$
$$\theta_{CO}^{1\times1}+\theta_O^{1\times1}+\theta_e^{1\times1}=1. \tag{8}$$

The rate equations[15] are given by

$$\frac{\partial(\theta_{CO}^{hex}\theta_{hex})}{\partial t} = k_1 p_{CO} S_{CO}^{hex}\theta_{hex}(1-\theta_{CO}^{hex}) - k_2\theta_{CO}^{hex}\theta_{hex} - k_4 B\theta_{CO}^{hex}(1-\theta_O^{1\times1}-\theta_{CO}^{1\times1}) + k_5 B\theta_{CO}^{1\times1}(1-\theta_{CO}^{hex}) + \min\left(0,-\theta_{CO}^{hex}\frac{\partial\theta_{1\times1}}{\partial t}\right)$$
$$+ \max\left(0,-0.8\theta_{CO}^{1\times1}\frac{\partial\theta_{1\times1}}{\partial t}\right) - D^{hex}\theta_{hex}\theta_{CO}^{hex}\nabla^2\theta_e^{hex} - D^{hex}\theta_{CO}^{hex}\nabla^2(\theta_{hex}\theta_e^{hex}) + D^{hex}\theta_{hex}\theta_e^{hex}\nabla^2\theta_{CO}^{hex}$$
$$+ D^{hex}\theta_e^{hex}\nabla^2(\theta_{hex}\theta_{CO}^{hex}), \tag{9}$$

$$\frac{\partial(\theta_{CO}^{1\times1}\theta_{1\times1})}{\partial t} = k_1 p_{CO} S_{CO}^{1\times1}\theta_{1\times1}(1-\theta_O^{1\times1}-\theta_{CO}^{1\times1}) - k_3\theta_{CO}^{1\times1}\theta_{1\times1} - k_7\theta_{CO}^{1\times1}\theta_O^{1\times1}\theta_{1\times1} + k_4 B\theta_{CO}^{hex}(1-\theta_O^{1\times1}-\theta_{CO}^{1\times1}) - k_5 B\theta_{CO}^{1\times1}(1$$
$$-\theta_{CO}^{hex}) + \max\left(0,1.25\theta_{CO}^{hex}\frac{\partial\theta_{1\times1}}{\partial t}\right) + \min\left(0,\theta_{CO}^{1\times1}\frac{\partial\theta_{1\times1}}{\partial t}\right) - D^{1\times1}\theta_{1\times1}\theta_{CO}^{1\times1}\nabla^2\theta_e^{1\times1} - D^{1\times1}\theta_{CO}^{1\times1}\nabla^2(\theta_{1\times1}\theta_e^{1\times1})$$
$$+ D^{1\times1}\theta_{1\times1}\theta_e^{1\times1}\nabla^2\theta_{CO}^{1\times1} + D^{1\times1}\theta_e^{1\times1}\nabla^2(\theta_{1\times1}\theta_{CO}^{1\times1}), \tag{10}$$

$$\frac{\partial(\theta_O^{1\times1}\theta_{1\times1})}{\partial t} = k_6 p_{O_2} S_{O_2}^{1\times1}\theta_{1\times1}(1-\theta_O^{1\times1}-\theta_{CO}^{1\times1})$$
$$- k_7\theta_{CO}^{1\times1}\theta_O^{1\times1}\theta_{1\times1} + \min\left(0,\theta_O^{1\times1}\frac{\partial\theta_{1\times1}}{\partial t}\right), \tag{11}$$

$$\frac{\partial\theta_{1\times1}}{\partial t} = \frac{1}{2}[k_8(\theta_{CO}^{hex})^n\theta_{hex} - k_9(1-c(\theta))\theta_{1\times1}]$$
$$- \frac{1}{2}[k_8(\theta_{CO}^{hex})^n\theta_{hex} + k_9(1-c(\theta))\theta_{1\times1}]\tanh[\kappa(1$$
$$- c(\theta))], \tag{12}$$

where p_{CO} and p_{O_2} are the partial pressures of CO and O_2, respectively, S_{CO}^{hex} and $S_{CO}^{1\times1}$ are the sticking probabilities of CO on the hex and 1×1 phases, respectively, $S_{O_2}^{1\times1}$ is the sticking probability of O_2 on the 1×1 surface, and D^{hex} and $D^{1\times1}$ are diffusionlike coefficients for CO on the hex and 1×1 phases, respectively.

The righthand side of Eq. (12) tends to $k_8(\theta_{CO}^{hex})^n\theta_{hex}$ for $c(\theta)\geq1$ and $-k_9(1-c(\theta))\theta_{1\times1}$ for $c(\theta)<1$, as $\kappa\to\infty$, and is, therefore, a smoothed version of the corresponding discontinuous equation of Gruyters *et al.*[21] We chose $\kappa=1000$ in order to approximate a discontinuous change. The function $c(\theta)$ is defined to be

$$c(\theta) = \frac{\theta_{CO}^{1\times1}}{\theta_{CO}^{crit}} + \frac{\theta_O^{1\times1}}{\theta_O^{crit}}, \tag{13}$$

where θ_{CO}^{crit} and θ_O^{crit} are defined in Table I.

Our updated model contains two sets of new terms: the terms involving $\partial\theta_{1\times1}/\partial t$ on the righthand sides of Eqs. (9)–(11) account for the effect of surface density changes, while the terms involving D^{hex} and $D^{1\times1}$ describe same-phase diffusion. We discuss the derivation of these new terms in detail in the following section.

Gas global coupling can easily be introduced to account for variations in the partial pressures of CO and O_2, which result from inflow and outflow of reactants as well as reaction. However, since gas global coupling was found to be insignificant in the very low pressure range that we consider, as shown by experiment,[1,4,18,19] we have chosen not to include it in our model and have considered the partial pressures to be fixed, independent of time. We note, however, that at intermediate pressures, long-range coupling through the gas phase is necessary for global rate oscillations on Pt{100} (Ref. 19) and at low pressures on Pt{110} single crystals and polycrystalline platinum foils.[26,27] Lele and Lauterbach[19] found for Pt{100} that the nonlinear phenomena involved at the low pressures investigated in our study are markedly different from those operating at intermediate pressures, where they concluded that the phase transition may no longer be the driving force for rate oscillations. They suggested instead a mechanism involving the formation of subsurface oxygen under these higher pressure conditions. The importance of subsurface oxygen in pattern formation at intermediate pressures has been confirmed by recent ellipsomicroscopy for surface imaging experiments.[25]

MESOSCOPIC MODEL

A detailed explanation of the surface density modification and diffusion terms introduced in our model are given in the following subsections. Our aim is to perform a numerical integration in space and time of Eqs. (9)–(12), leading to a spatiotemporal description of the reactive process. In order to include diffusion, we divide the surface domain of integration into a grid of cells, as shown in Fig. 2, each containing

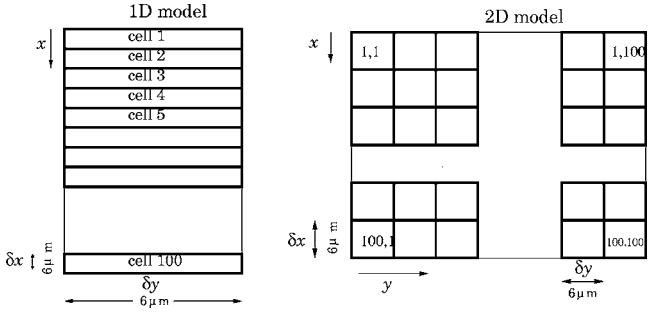

FIG. 2. The division of the surface into cells. Left: 1D cell model. Right: 2D model.

many CO adsorption sites. The cell size is intermediate between that of incipient hex and 1×1 phase patches and the much longer scale on which pattern formation occurs. We refer to models involving diffusion between cells along the x axis only as one dimensional (1D), while those permitting diffusion along both x and y axes are two dimensional (2D), where x and y refer to the dimensions in the cell length and width directions, respectively.

The 1D integrations are performed on a ribbon of area $A=L\delta x\delta y=3600\ \mu\mathrm{m}^2$, where $L=100$, while the 2D integrations are performed on a domain of length $L\delta x$ and width $L\delta y$, with area $A=L^2\delta x\delta y=3.6\times10^5\ \mu\mathrm{m}^2$. The domain is taken to be spatially periodic in the x direction in the 1D case, and in both x and y directions in the 2D case: in other words, there is a repeat of the domain and the surface patterns within it at each boundary. The numerical integration uses Adams-Bashforth time stepping and second-order spatial finite differences. The same-phase diffusion leads to spatial coupling between cells and is derived below for the case where δx and δy are equal.

Surface density changes at phase change

The adsorbate-induced hex to 1×1 phase change described by Eq. (12) for $c(\theta)\geqslant1$ leads to a change in the density of surface sites and, hence, to a change in the fraction of sites occupied by CO in each of the two phases. Equations (9)–(11) include terms that take this into account. At phase change on a crystal of area A, in a short time interval δt, an area $A\,\delta\theta_{1\times1}$ of 1×1 surface is created and a corresponding area, $A(-\delta\theta_{\mathrm{hex}})=A\,\delta\theta_{1\times1}$, of hex surface is destroyed. The area taken up by CO on the destroyed hex surface was $A\theta_{\mathrm{CO}}^{\mathrm{hex}}(-\delta\theta_{\mathrm{hex}})=A\theta_{\mathrm{CO}}^{\mathrm{hex}}\delta\theta_{1\times1}$. This is lost in the surface restructuring, so the change in the area covered by CO on hex phase is $\delta(A\theta_{\mathrm{CO}}^{\mathrm{hex}}\theta_{\mathrm{hex}})=-A\theta_{\mathrm{CO}}^{\mathrm{hex}}\delta\theta_{1\times1}$. Therefore, from the phase change alone we have

$$\frac{\partial(\theta_{\mathrm{CO}}^{\mathrm{hex}}\theta_{\mathrm{hex}})}{\partial t}=-\theta_{\mathrm{CO}}^{\mathrm{hex}}\frac{\partial\theta_{1\times1}}{\partial t}. \tag{14}$$

The additional area occupied by the CO on the 1×1 phase (assuming that all displaced CO from the destroyed hex patch ends up on the 1×1 phase) is $A\theta_{\mathrm{CO}}^{\mathrm{hex}}\delta\theta_{1\times1}a_{1\times1}/a_{\mathrm{hex}}$, where $a_{1\times1}$ is the area occupied by a 1×1 site and a_{hex} is the area occupied by a hex site. We take $a_{1\times1}/a_{\mathrm{hex}}$ to be about 1.25, since about 20% of atoms are displaced during the phase change[28] and $1/0.8=1.25$. Hence, from the phase change alone, we have

$$\frac{\partial(\theta_{\mathrm{CO}}^{1\times1}\theta_{1\times1})}{\partial t}=1.25\theta_{\mathrm{CO}}^{\mathrm{hex}}\frac{\partial\theta_{1\times1}}{\partial t}. \tag{15}$$

The process is reversed during the relaxation of the 1×1 surface to hex phase, described by Eq. (12), when $c(\theta)<1$ and $\partial\theta_{1\times1}/\partial t$ is negative. Now, the CO is displaced from a destroyed 1×1 patch onto a newly formed hex patch, and the terms that describe this reverse process can be shown in similar fashion to be

$$\frac{\partial(\theta_{\mathrm{CO}}^{\mathrm{hex}}\theta_{\mathrm{hex}})}{\partial t}=-0.8\theta_{\mathrm{CO}}^{1\times1}\frac{\partial\theta_{1\times1}}{\partial t} \tag{16}$$

in Eq. (9), where the factor of 0.8 is given by $a_{\mathrm{hex}}/a_{1\times1}$, and

$$\frac{\partial(\theta_{\mathrm{CO}}^{1\times1}\theta_{1\times1})}{\partial t}=\theta_{\mathrm{CO}}^{1\times1}\frac{\partial\theta_{1\times1}}{\partial t} \tag{17}$$

in Eq. (10). The combined effect of the forward and backward transitions between hex and 1×1 is

$$\frac{\partial(\theta_{\mathrm{CO}}^{\mathrm{hex}}\theta_{\mathrm{hex}})}{\partial t}=\min\left(0,-\theta_{\mathrm{CO}}^{\mathrm{hex}}\frac{\partial\theta_{1\times1}}{\partial t}\right)+\max\left(0,-0.8\theta_{\mathrm{CO}}^{1\times1}\frac{\partial\theta_{1\times1}}{\partial t}\right), \tag{18}$$

$$\frac{\partial(\theta_{\mathrm{CO}}^{1\times1}\theta_{1\times1})}{\partial t}=\max\left(0,1.25\theta_{\mathrm{CO}}^{\mathrm{hex}}\frac{\partial\theta_{1\times1}}{\partial t}\right)+\min\left(0,\theta_{\mathrm{CO}}^{1\times1}\frac{\partial\theta_{1\times1}}{\partial t}\right). \tag{19}$$

The coverage of oxygen is not affected by the adsorbate-induced restructuring since oxygen does not stick to hex surface, so no oxygen can be displaced from it as it is destroyed. However, during the relaxation, when 1×1 surface is replaced by hex, any oxygen on the destroyed 1×1 patch is assumed to be released as gas, and so we have a contribution,

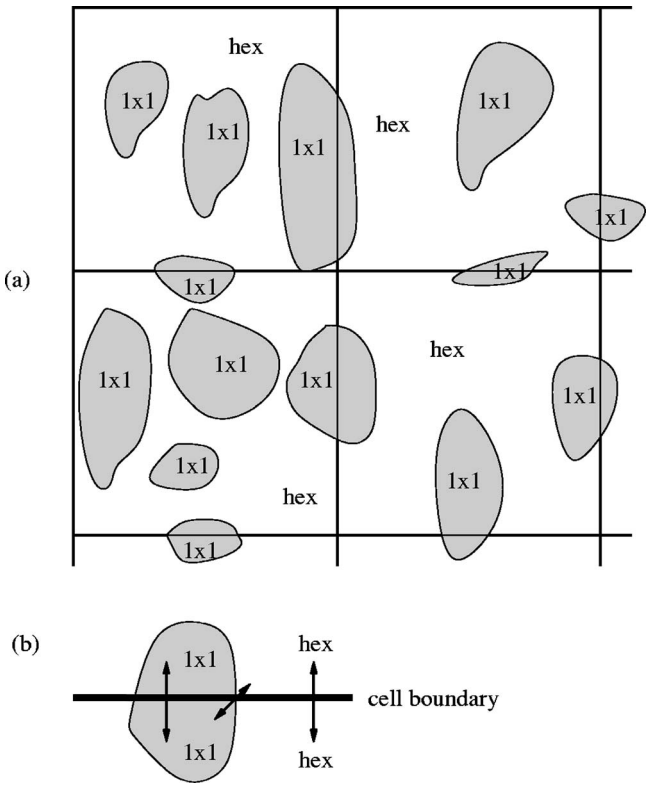

FIG. 3. (a) 1×1 islands growing on a hex surface, with the mesoscopic lattice of cells superimposed. (The size of the islands relative to the cells is exaggerated for clarity.) (b) CO diffusion at the boundary between two neighboring cells. Arrows indicate same-phase and cross-phase diffusions from one cell to another. Same-phase diffusion is dominant because most of the boundary lies within a single patch rather than on the boundary between 1×1 and hex patches.

$$\frac{\partial(\theta_{\mathrm{O}}^{1\times1}\theta_{1\times1})}{\partial t} = \min\left(0, \theta_{\mathrm{O}}^{1\times1}\frac{\partial\theta_{1\times1}}{\partial t}\right), \tag{20}$$

in Eq. (11). The min function is used to ensure that the term is only effective when $\partial\theta_{1\times1}/\partial t$ is negative.

Same-phase diffusion

Carbon monoxide can diffuse on both hex and 1×1 surfaces, whereas oxygen is relatively immobile at the temperatures used in our model. The dominant contribution from CO diffusion will come from molecules moving from one hex site to another nearby hex site or from a 1×1 site to another 1×1 site. This is because hex and 1×1 sites are only close enough together for diffusion to occur between them at the boundaries of patches, and most sites lie in the interior of a patch rather than on the boundary (see Fig. 3).

Hence, for diffusion on the hex phase, a CO molecule must be untrapped at one hex site and retrapped at another hex site nearby. Most of the CO that is untrapped will be retrapped in the same cell, but let us say that a certain proportion ϵ migrates between cells. (In what follows, we consider the 2D model; the 1D case is analogous.) The rate of untrapping in the donor cell (i,j) will be proportional to the density of CO on the hex phase there, $\theta_{\mathrm{CO}(i,j)}^{\mathrm{hex}}$, and the rate of retrapping in the nearest neighbor (up, down, left, and right) cells (nn) will be proportional to the density of empty sites on the hex phase there, $1-\theta_{\mathrm{CO}(nn)}^{\mathrm{hex}}$. In a short time interval δt, the net change in CO coverage on the hex phase in cell (i,j) owing to diffusion alone is given by

$$\delta(\theta_{\mathrm{CO}}^{\mathrm{hex}}\theta_{\mathrm{hex}})_{(i,j)} = -k\epsilon\theta_{\mathrm{CO}(i,j)}^{\mathrm{hex}}\sum_{(nn)}\theta_{e(nn)}^{\mathrm{hex}}\delta t + k\epsilon\theta_{e(i,j)}^{\mathrm{hex}}\sum_{(nn)}\theta_{\mathrm{CO}(nn)}^{\mathrm{hex}}\delta t, \tag{21}$$

where k is a constant of proportionality that is related to the speed of unhindered CO migration on the hex phase. This accounts for CO leaving the cell (i,j) and CO arriving from cells (nn). Now, ϵ is proportional to the amount of cell boundary that is within a hex patch, which will be proportional to the coverage of hex phase, θ_{hex}, in the current patch (i,j). Since we are modeling diffusion at the boundary between cells, we take the average of the coverage in cell (i,j) and the nearest neighbor cell (nn).

$$\delta(\theta_{\mathrm{CO}}^{\mathrm{hex}}\theta_{\mathrm{hex}})_{(i,j)} = -K\sum_{(nn)}(\theta_{\mathrm{hex}(i,j)}+\theta_{\mathrm{hex}(nn)})\theta_{\mathrm{CO}(i,j)}^{\mathrm{hex}}\theta_{e(nn)}^{\mathrm{hex}}\delta t + K\sum_{(nn)}(\theta_{\mathrm{hex}(i,j)}+\theta_{\mathrm{hex}(nn)})\theta_{e(i,j)}^{\mathrm{hex}}\theta_{\mathrm{CO}(nn)}^{\mathrm{hex}}\delta t, \tag{22}$$

where K is once more a constant of proportionality that is related to the speed of migration of CO on clean hex phase. Adding and subtracting $8K\theta_{\mathrm{hex}(i,j)}\theta_{\mathrm{CO}(i,j)}^{\mathrm{hex}}\theta_{e(i,j)}^{\mathrm{hex}}$, we can rearrange this equation to get

$$\delta(\theta_{\mathrm{CO}}^{\mathrm{hex}}\theta_{\mathrm{hex}})_{(i,j)} = -K\theta_{\mathrm{hex}(i,j)}\theta_{\mathrm{CO}(i,j)}^{\mathrm{hex}}\sum_{(nn)}(\theta_{e(nn)}^{\mathrm{hex}}-\theta_{e(i,j)}^{\mathrm{hex}})\delta t - K\theta_{\mathrm{CO}(i,j)}^{\mathrm{hex}}\sum_{(nn)}(\theta_{\mathrm{hex}(nn)}\theta_{e(nn)}^{\mathrm{hex}}-\theta_{\mathrm{hex}(i,j)}\theta_{e(i,j)}^{\mathrm{hex}})\delta t + K\theta_{\mathrm{hex}(i,j)}\theta_{e(i,j)}^{\mathrm{hex}}\sum_{(nn)}(\theta_{\mathrm{CO}(nn)}^{\mathrm{hex}}-\theta_{\mathrm{CO}(i,j)}^{\mathrm{hex}})\delta t + K\theta_{e(i,j)}^{\mathrm{hex}}\sum_{(nn)}(\theta_{\mathrm{hex}(nn)}\theta_{\mathrm{CO}(nn)}^{\mathrm{hex}}-\theta_{\mathrm{hex}(i,j)}\theta_{\mathrm{CO}(i,j)}^{\mathrm{hex}})\delta t. \tag{23}$$

Now, if we set $K=D^{\mathrm{hex}}/\delta x^2$, divide by δt, and take the limits as $\delta x\to0$ and $\delta t\to0$, we get

$$\frac{\partial}{\partial t}(\theta_{\mathrm{CO}}^{\mathrm{hex}}\theta_{\mathrm{hex}}) = -D^{\mathrm{hex}}\theta_{\mathrm{hex}}\theta_{\mathrm{CO}}^{\mathrm{hex}}\nabla^2\theta_e^{\mathrm{hex}} - D^{\mathrm{hex}}\theta_{\mathrm{CO}}^{\mathrm{hex}}\nabla^2(\theta_{\mathrm{hex}}\theta_e^{\mathrm{hex}}) + D^{\mathrm{hex}}\theta_{\mathrm{hex}}\theta_e^{\mathrm{hex}}\nabla^2\theta_{\mathrm{CO}}^{\mathrm{hex}} + D^{\mathrm{hex}}\theta_e^{\mathrm{hex}}\nabla^2(\theta_{\mathrm{hex}}\theta_{\mathrm{CO}}^{\mathrm{hex}}) \tag{24}$$

as the contribution from hex phase diffusion alone. D^{hex} is a diffusionlike coefficient. Taking the limits as $\theta_e^{\mathrm{hex}}\to1$ and $\theta_{\mathrm{hex}}\to1$ shows that D^{hex} is equal to half the diffusion coefficient for CO on clean hex phase. A similar analysis for the 1×1 phase gives

$$\frac{\partial}{\partial t}(\theta_{\mathrm{CO}}^{1\times1}\theta_{1\times1}) = -D^{1\times1}\theta_{1\times1}\theta_{\mathrm{CO}}^{1\times1}\nabla^2\theta_e^{1\times1} - D^{1\times1}\theta_{\mathrm{CO}}^{1\times1}\nabla^2(\theta_{1\times1}\theta_e^{1\times1}) + D^{1\times1}\theta_{1\times1}\theta_e^{1\times1}\nabla^2\theta_{\mathrm{CO}}^{1\times1} + D^{1\times1}\theta_e^{1\times1}\nabla^2(\theta_{1\times1}\theta_{\mathrm{CO}}^{1\times1}), \tag{25}$$

where, as expected, $D^{1\times1}$ is equal to half the diffusion coefficient for CO on clean 1×1 phase. For our simulations we used the values $D^{\mathrm{hex}}=D^{1\times1}=10^{-6}$ cm^2 s^{-1} since the diffusion coefficient of adsorbed CO is estimated to be of the order of 10^{-6} cm^2 s^{-1}.[2]

RESULTS: 1D MODEL

We used two sets of initial conditions, given in Table II, both describing a surface that was inhomogeneous in terms of the local coverage of the adsorbate reactants on the two

TABLE II. Initial conditions used in the 1D simulations summarized in Fig. 4.

	Cell no.	Fig. 4(a)	Fig. 4(b)
		Bulk surface	
$\theta_{1\times1}$		10^{-3}	0.735
$\theta_{O}^{1\times1}$		0	2.98×10^{-4}
$\theta_{CO}^{1\times1}$		0	0.402
θ_{CO}^{hex}		0	3.54×10^{-2}
		Defects	
$\theta_{CO}^{1\times1}$		0	0.340 979
θ_{CO}^{hex}		0	0.019 829
$\theta_{1\times1}$	1	0.5	0.834
	38	0.5	0.734
	56	0.9	0.234
	89	0.9	⋯
$\theta_{O}^{1\times1}$	1	0.5	1.10×10^{-3}
	38	1.0	1.10×10^{-3}
	56	0.5	1.10×10^{-3}
	89	1.0	⋯

phases of Pt{100}. A number of surface defects (inhomogeneities) of dimension $\delta x\delta y=36\ \mu m^2$ were mimicked in the 1D model by choosing the initial coverage conditions in certain cells to differ from those of the rest of the surface (see Table II) in order to model the effect of local differences in topography and sticking probablities. One could also model defects by, for example, modifying the sticking probabilities permanently in certain locations, but we would not expect this to alter the types and speeds of fronts observed that are our focus in this study, as these are determined by the properties of the rate equations on the bulk surface—the defects simply start them off. On the other hand, one would expect to see successive waves of fronts emerging from such persistent defects. As it is not clear exactly how to mimic defects we decided to choose a method that has the least impact on the long-term results.

A systematic exploration of the behavior of the system as a function of partial pressures was performed at a fixed surface temperature of 480 K. For the simulations summarized in Fig. 4(a), the integration time was 1000 s, while those described in Fig. 4(b) were continued for up to 4000 s in order to determine whether long-period oscillations were present.

The presence of initial surface inhomogeneities was found to affect the behavior of the system crucially and, under certain conditions of reactant partial pressures, to lead to the formation of traveling waves. In experiments, the temporal variation of the reaction rate was found to parallel that of the work function, $\Delta\phi$. The latter has, therefore, been used to monitor the occurrence of oscillatory behavior, as measured by a Kelvin probe.[1,16,18] The experimental parameter range for sustained temporal oscillations was mapped by Eiswirth *et al.*[1] by varying the partial pressures of O_2 and CO (p_{O_2} and p_{CO}) at a constant surface temperature of 480 K. Three distinct regions of phase space were found in their study and are summarized in Fig. 4, alongside those obtained by our model. Maximum amplitudes were established under

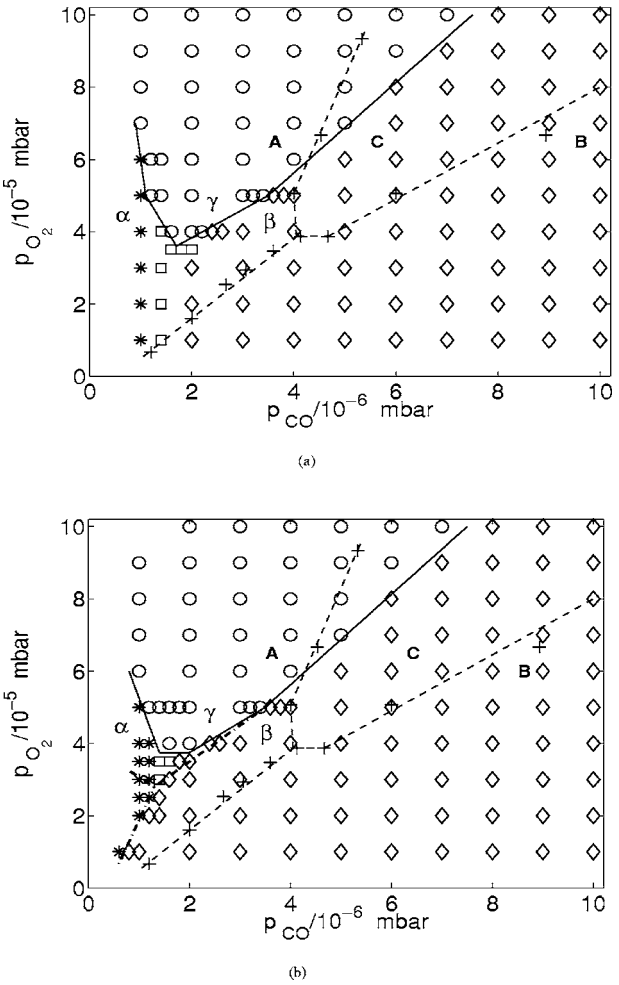

FIG. 4. The existence regime for sustained oscillations in our model ($^*/\square/\diamond/\bigcirc$ and solid lines) for the two sets of initial conditions given in Table II, compared with experimental observations (Ref. 1) (+ and dashed lines). (a) also appears as Fig. 1 of Ref. 15 [Hoyle, Anghel, Proctor, and King, Phys. Rev. Lett. **98**, 226102 (2007)]. "Copyright (2007) by the American Physical Society." Key: $^*/\square/\diamond$, steady evolution to low/medium/high CO state and $\bigcirc$, regular surface oscillations. In simulations, region α corresponds to low CO and 1×1 coverages, region β to high CO and 1×1 coverages, and region γ to oscillations. The solid lines show the oscillation regime defined using a cutoff of 1000 s for the oscillation period and in (b), the region defined using a 3000 s cutoff is marked by dashed-dotted lines. Experimental regions A, B, and C (Ref. 1) are defined by surfaces showing low and high CO coverages and oscillations, respectively.

experimental conditions whenever the CO pressure was adjusted in such a way that the CO coverage in a CO atmosphere alone would be around $\theta_{CO}=0.5$. Furthermore, a decrease in p_{CO} and temperature was found to be associated with an increase in the oscillation period.[18] Oscillations were never found below $p_{CO}=3\times10^{-6}$ Torr (Ref. 1) at the range of surface temperatures investigated and were found to be mainly irregular in nature, with few regions exhibiting regular oscillatory behavior.[4,17–19] The irregularity of the oscillations suggests that they are not in phase across the whole surface and might signal the presence of traveling waves or other spatial patterns.

The results of our model simulations also divide the parameter space of reactant partial pressures (p_{O_2} and p_{CO}) into three regions defined by solid lines in Fig. 4, which can be thought of roughly as low CO-coverage states (region α),

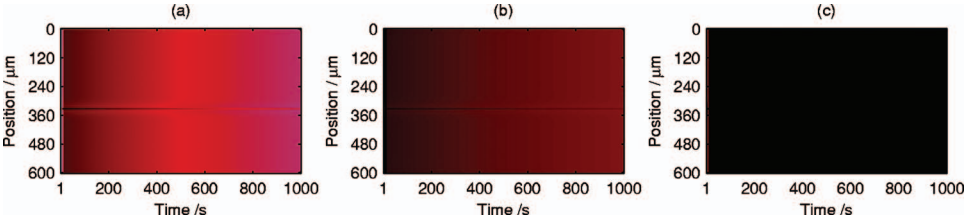

FIG. 5. (Color) Steady evolution to a low CO state at $p_{O_2}=3\times10^{-5}$ mbar and $p_{CO}=1\times10^{-6}$ mbar with the same initial conditions as for Fig. 4(b). Space-time diagrams for (a) 1×1, (b) total CO, and (c) total O coverages; at $t=2999$ s, typical values for these are 0.51, 0.19, and 1.3×10^{-4}, respectively. Colorscale: 0.0=black<red<blue<yellow<white=1.0.

high CO-coverage states (region β), and oscillatory states (region γ). Below, we discuss the types of solution to be found in each region (illustrated in Figs. 5–10), characterizing them by the total carbon monoxide and oxygen coverages of the surface, $\theta_{1\times1}\theta_{CO}^{1\times1}+\theta_{hex}\theta_{CO}^{hex}$ and $\theta_{1\times1}\theta_{O}^{1\times1}$, respectively.

Region α, where p_{CO} is low, corresponds to solutions that evolve steadily to surfaces with low 1×1 and low total CO coverages. The final low CO state in Fig. 5 (total CO coverage of 0.19 at $t=2999$ s) also has comparatively low 1×1 coverage (0.51) and very low total oxygen coverage (1.3×10^{-4}).

Region β, corresponding to high values of p_{CO} to the right of region γ, is characterized by homogeneously high 1×1 coverages, with very low total oxygen coverages and comparatively high total CO coverages. For example, the simulation shown in Fig. 6 has typical values of 0.93, 0.38, and 7.0×10^{-5} for the 1×1, total CO, and total oxygen coverages, respectively, at time $t=999$ s. These high CO solutions typically approach their final coverages much more rapidly than the low CO states in region α.

Region γ contains regular surface oscillations (Fig. 7); it is V shaped and tilted toward higher values of p_{CO}. The range of oscillation periods was roughly 80–2700 s, with shorter periods in the midrange of p_{CO} and for higher values of p_{O_2}. It is not obvious how to distinguish between very long-period oscillations (that might not be easy to observe experimentally) and steady evolution. In Fig. 4(a), we assumed that any solution that had not repeated within 1000 s was steady, and in Fig. 4(b), we compared 1000 and 3000 s cutoffs. As can be seen in Fig. 4(b), a lower threshold for the period pushes the triple point between regions α, β, and γ toward higher values of the two reactant partial pressures, improving the match with experimental data.[1] This could be explained if very long-period oscillations were hard to observe experimentally. On the other hand, longer integration times lead to a clear distinction between regions α and β below region γ [shown as a dotted-dashed line in Fig. 4(b)] as in experiment. This is replaced by a transition via medium-CO solutions when simulations are run only for 1000 s [solid line in Figs. 4(a) and 4(b)].

We saw two types of propagating front in our simulations, which we denote as CO and oxygen-CO. The CO fronts are found for the full range of partial pressures, provoked early on by low $\theta_{1\times1}$, $\theta_{O}^{1\times1}$, θ_{CO}^{hex}, and medium/high $\theta_{CO}^{1\times1}$ defects in surfaces where $\theta_{1\times1}$ was initially high. Since the CO fronts move quite slowly, we had to use finer 200×200 or 200×1 grids in order to measure their progress with sufficient accuracy that we could capture their speeds to within 10%. For low p_{CO} and p_{O_2} of 3.5×10^{-5} mbar and above in Fig. 4(b), we have a CO front, followed by small-amplitude oscillations. The period of the ensuing oscillations is longer for lower p_{O_2} and lower p_{CO} (in agreement with experiment[18]). We also performed simulations using bulk initial conditions $\theta_{1\times1}=0.7$, $\theta_{O}^{1\times1}=0.95$, and $\theta_{CO}^{1\times1}=\theta_{CO}^{hex}=0.01$, with defects of $\theta_{1\times1}=\theta_{O}^{1\times1}=\theta_{CO}^{hex}=0.01$ and $\theta_{CO}^{1\times1}=0.45$, and found a range of CO front speeds from 0.13 to 14 μm s^{-1} compared with 2–50 μm s^{-1} experimentally.[2,4,19] For the example in Fig. 8, the speed is approximately 0.3 μm s^{-1}. We see that the surface initially has high 1×1 and total oxygen coverages, with an insignificant total coverage of CO. The defects provoke waves of CO, at quite modest coverage, which spread out and displace the oxygen ahead. Phase relaxation takes place at the leading edge of the front, so the surface is predominantly in the hex phase behind it. Once the front has passed, there are low-amplitude oscillations in the coverages behind it, with the total CO coverage remaining low and the total oxygen coverage negligible. For high p_{O_2} and low p_{CO} in Fig. 4(b), the CO fronts travel until they meet another such front but as we approach $p_{O_2}=3.5\times10^{-5}$ mbar, they become localized close to the original de-

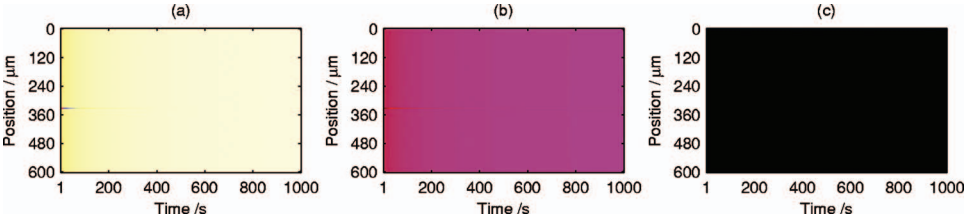

FIG. 6. (Color) Steady evolution to a high CO state at $p_{O_2}=2\times10^{-5}$ mbar and $p_{CO}=3\times10^{-6}$ mbar with the same initial conditions as for Fig. 4(b). Space-time diagrams for (a) 1×1, (b) total CO, and (c) total O coverages; at $t=999$ s, typical values for these are 0.93, 0.38, and 7.0×10^{-5}, respectively. Colorscale is the same as for Fig. 5.

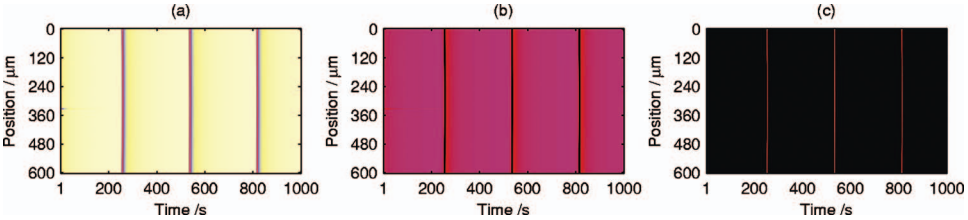

FIG. 7. (Color) Regular surface oscillations at $p_{O_2}=7\times10^{-5}$ mbar and $p_{CO}=4\times10^{-6}$ mbar with the same initial conditions as for Fig. 4(b). Space-time diagrams for (a) 1×1, (b) total CO, and (c) total O coverages. Colorscale is the same as for Fig. 5.

fect and very short-lived. For the initial conditions used in Fig. 8, higher p_{CO} and lower p_{O_2} lead to lower total oxygen coverage ahead of the front and higher $\theta_{1\times1}$ and total CO coverages behind it, so the phase relaxation is less marked (though, there is still a pronounced dip in 1×1 coverage at the leading edge of the front, even when it recovers behind) and the CO fronts move faster, supporting the argument[4,19] that the relatively slow speed of CO waves arises from the phase transition at the front.

Oxygen-CO fronts are also triggered by defects and consist of a wave of CO following closely on the heels of an oxygen wave. They are found on the lefthand side of region γ at high p_{O_2}. When p_{O_2} is lower, they can occur for values of p_{CO} on either side of region γ and also on the border between regions α and β, depending on the initial conditions. In region γ, the fronts are followed by oscillations. The wave speed and oscillation period are correlated: where the oscillations are faster or slower, so are the preceding waves. In our simulations, both CO and oxygen-CO fronts often coexist with oscillations, so the overall reaction rate or work function oscillations will appear irregular, as is typically observed.[4,17–19] Figures 10(d)–10(f) show an oxygen front (triggered by the defect in cell 1) at the sides of the domain, moving into an initial solution with high 1×1, medium total CO, and very low total oxygen coverages. The reaction wave removes the adsorbed CO, and there is some phase relaxation at the front so the 1×1 coverage falls. A wave of CO follows a few seconds later [Figs. 10(g)–10(i)], removing the oxygen in turn. After the two consecutive waves have passed, the surface recovers to its initial state. Similar combinations of oxygen and CO fronts have been observed in experiment [see Fig. 6 of Ref. 4 (which also appears as Fig. 3 of Ref. 19)]. During phase relaxation the 1×1 coverage does not fall as far as for the CO fronts discussed above, so the speed of the simulated oxygen-CO fronts is higher[4,19] in the range of 13–90 μm s^{-1}. The oxygen front shown in Fig. 10 is moving at approximately 37 μm s^{-1} and the speed of the subsequent CO front is about 36 μm s^{-1}. In comparison, Lauterbach and Rotermund[4] measured CO front speeds between 2 and 26 μm s^{-1} and oxygen front speeds between 50 and 240 μm s^{-1}, though they were working at slightly higher partial pressures than we have used.

Comparing Figs. 4(a) and 4(b) shows the importance of initial conditions. Hysteresis appears to be present in the simulations in that the bulk initial conditions influence the state of the surface at long times and can shift the boundaries between regions α, β, and γ, with low initial CO coverage moving them toward higher p_{CO} and vice versa. Experimentally, p_{CO} was repeatedly increased and decreased in order to confirm the extent of region C: this led to large error bars on the position of the boundaries (not shown in Fig. 4), suggesting that the history of the partial pressures and surface state is indeed important. We found that the choice of defect initial conditions typically determines the initial transient behavior, for instance, provoking front propagation (Fig. 8). However, it is possible for the effect of defects to be long lasting. Figure 11(a) shows a simulation at $p_{CO}=6\times10^{-7}$ mbar and $p_{O_2}=1\times10^{-5}$ mbar with the same initial conditions as for

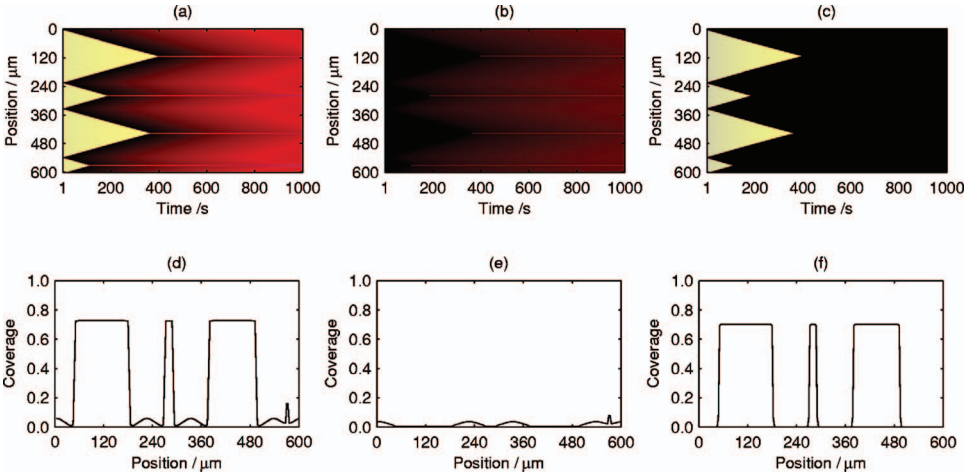

FIG. 8. (Color) CO front at $p_{O_2}=6\times10^{-5}$ mbar and $p_{CO}=1\times10^{-6}$ mbar with bulk initial conditions $\theta_{1\times1}=0.7$, $\theta_O^{1\times1}=0.95$, and $\theta_{CO}^{1\times1}=\theta_{CO}^{hex}=0.01$ and defects, where $\theta_{1\times1}=\theta_O^{1\times1}=\theta_{CO}^{hex}=0.01$ and $\theta_{CO}^{1\times1}=0.45$ in cells 1–2, 75–76, 111–112, and 179–180. Space-time diagrams for (a) 1×1, (b) total CO, and (c) total O coverages. Colorscale is the same as for Fig. 5. Snapshots at time $t=149$ s for (d) 1×1, (e) total CO, and (f) total O coverages.

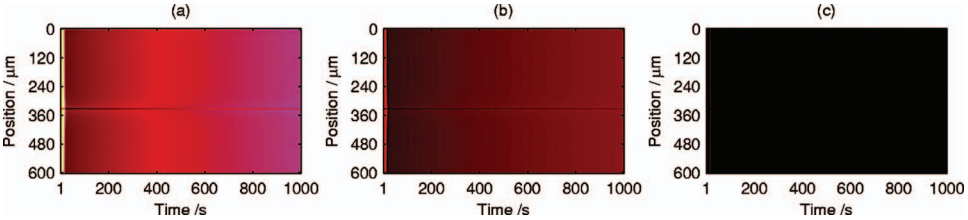

FIG. 9. (Color) Oxygen front followed by CO front followed by steady evolution to low CO state at $p_{O_2}=2\times10^{-5}$ mbar and $p_{CO}=1\times10^{-6}$ mbar with the same initial conditions as for Fig. 4(b). Space-time diagrams for (a) 1×1, (b) total CO, and (c) total O coverages. Colorscale is the same as for Fig. 5.

Fig. 4(b), and Fig. 11(b) shows the effect of changing $\theta_{1\times1}$ in cell 1 to 0.01 from 0.834. The long-term 1×1 coverage is changed from fairly uniformly low to a profile that varies between low and medium across the surface. We did not find any other persistent effects of defects (though, neither did we carry out an exhaustive search) and hypothesize that in this case, proximity to the region α/β border may be important.

We now compare the results of our model with experiment. Eiswirth *et al.*[1] found two nonoscillating regions, A and B and an intermediate region where oscillations in the work function were observed. The existence region for self-sustaining work function oscillations, labeled as C is V shaped with a tilt toward higher CO pressures, in agreement with our model region γ. However, the experimental region is shifted to higher p_{CO} pressures compared to our model. This might arise from a difference in the way the partial pressures were set: while the values of p_{CO} and p_{O_2} are fixed throughout each of our simulations, the experimental protocol[1] involved setting p_{O_2} to a constant value and initially increasing p_{CO} in steps. The position of the experimental region was then determined in both directions by repeatedly increasing and decreasing p_{CO}. The error bars in p_{CO} for the boundary position were large. Taking into account the initial stepwise increase, it is likely that the average value of p_{CO} over a single run was lower than the final value used in plotting the experimental region and perhaps, this is important. If the experimental region were plotted using this lower average p_{CO} value, it would be shifted toward lower p_{CO}, possibly closer to our model region γ. The triple point between the three regions is also at lower p_{O_2} in our model, compared to experiment, if we use a 3000 s cutoff to distinguish between steady and oscillatory solutions. Adopting a lower period cutoff for distinguishing between oscillatory and steady structures corrects this [Fig. 4(b)], but at the expense of designating some solutions we know to be periodic as steady. However, it seems likely that very long-period oscillations would be hard to observe experimentally as they would be vulnerable to disruption by small fluctuations in experimental conditions. Although, we stated when introducing the kinetic rate equations that adopting over the whole 1×1 surface the (higher) oxygen sticking probability for freed rather than "free" sites makes little difference in our model, it is likely to be a reason for the shift of the triple point to lower p_{O_2} since this is very sensitive to small

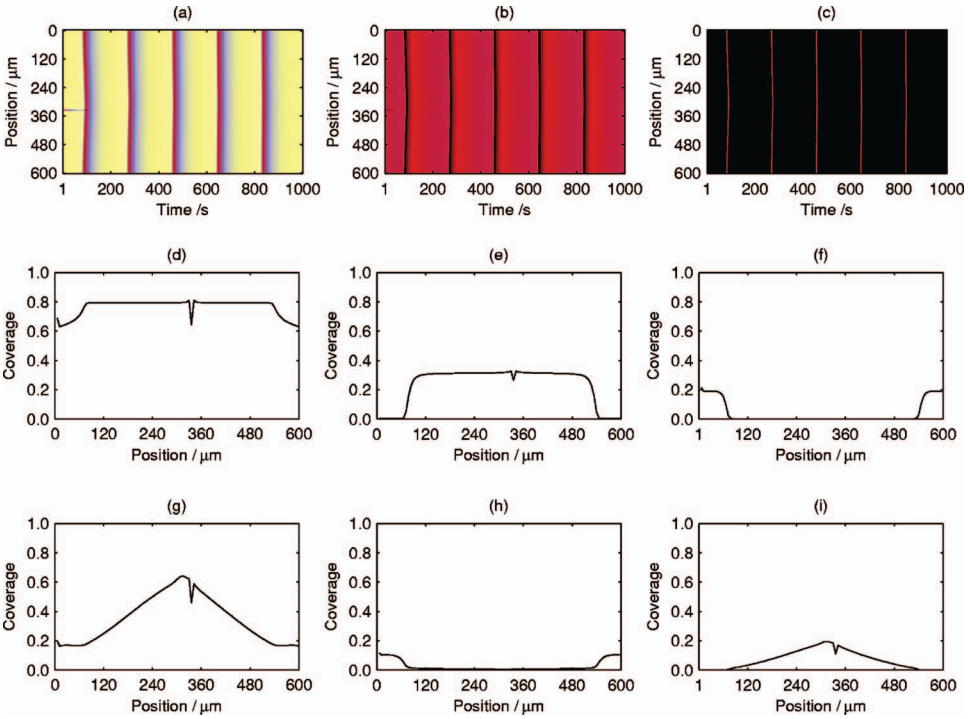

FIG. 10. (Color) Oxygen front followed by CO front at $p_{O_2}=7\times10^{-5}$ mbar and $p_{CO}=3\times10^{-6}$ mbar with the same initial conditions as for Fig. 4(b). Space-time diagrams for (a) 1×1, (b) total CO, and (c) total O coverages. Colorscale is the same as for Fig. 5. Snapshots at time $t=82$ s for (d) 1×1, (e) total CO, and (f) total O coverages and [(g)–(i)] at time $t=90$ s.

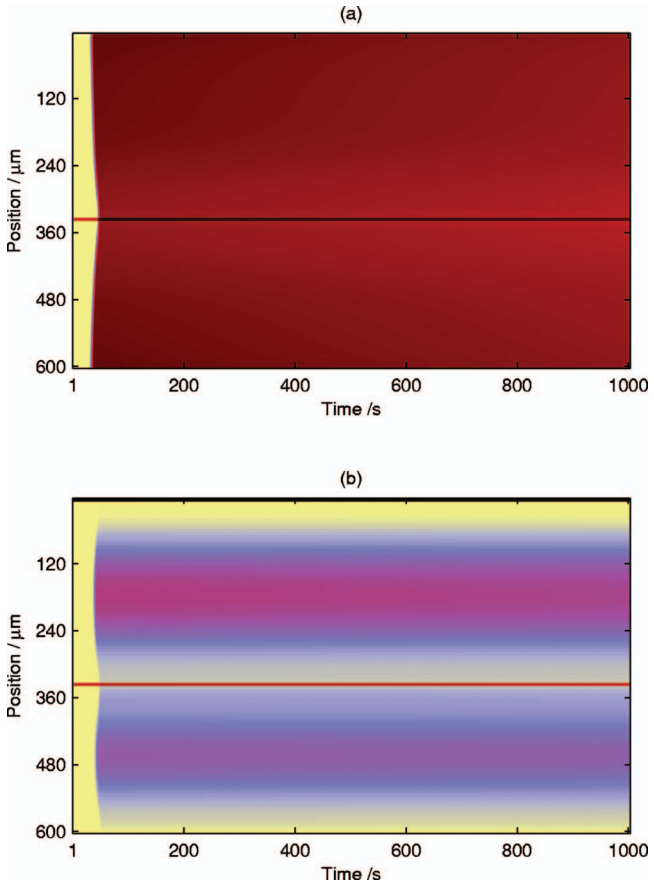

FIG. 11. (Color) The effect of changing $\theta_{1\times1}$ from (a) 0.834 to (b) 0.01 in cell 1 is long lasting at $p_{O_2}=1\times10^{-5}$ mbar and $p_{CO}=6\times10^{-7}$ mbar with the same remaining initial conditions as for Fig. 4(b). Space-time diagrams are shown for the 1×1 coverage. Colorscale is the same as for Fig. 5.

changes in the experimental conditions and the cutoff values chosen. Finally, the presence of a traveling wave component in many of our oscillatory solutions fits with the experimental observation that work function oscillations are typically irregular.[4,17–19]

For experimental region A, where the CO pressure is very low, the work function was found to be constant and high, which was interpreted in terms of excess oxygen being present on the surface. This region matches well with the results within region α from our model, where solutions show high total oxygen coverage (e.g., before the passing of the CO front in Fig. 8) and/or relatively low coverage of chemisorbed CO that does not hinder uptake of oxygen at the surface. For region B, the work function was found to be low and constant. This has been interpreted in terms of a high CO coverage that inhibits O_2 adsorption, again in agreement with region β in our theory model.

In experiments, the periods for self-sustaining oscillations with amplitudes in $\Delta\phi$ between 100 and 300 mV ranged typically between 1 and 4 min at temperatures around 500 K, while at lower temperatures, periods of up to 10 min and longer were observed. Faster oscillations, with periods as short as a few seconds, were found at small amplitudes.[18] Our model also finds a wide range of oscillation periods within the mapped region γ, from 80 s to 45 min, with the fastest oscillations being found in the midrange of p_{CO} and for higher p_{O_2}. The oscillations in our simulations appear to be of somewhat longer period than those observed experimentally, though the partial pressures we used were typically somewhat lower, which may account for the difference. In the next section, we discuss our 2D simulations and compare the carbon monoxide and oxygen-CO fronts we see with those observed experimentally during pattern formation.

RESULTS: 2D MODEL

A two-dimensional CO front is shown in Fig. 12 for the same partial pressures as the 1D case illustrated in Fig. 8. Reaction fronts can be seen propagating outwards from defects at an initial speed of approximately 0.24 μm s^{-1}. Initially, the fronts are approximately circular, but they become distorted as they interact. Ahead of the wave, the surface is predominantly covered by oxygen on 1×1 phase, while behind it, the surface is in hex phase with no adsorbed oxygen and a modest coverage of CO. We would expect oscillations at low 1×1 and CO coverages in the wake of the front, as in the 1D case. The initial wave speed is 0.24 μm s^{-1}, which is a little slower than for the 1D case. This is possibly due to the curved shape of the 2D front and the influence of other nearby fronts.

In order to investigate the structure of two-dimensional oxygen-CO fronts, we present a series of snapshots (Fig. 13) of the 1×1, total CO, and total oxygen coverages between

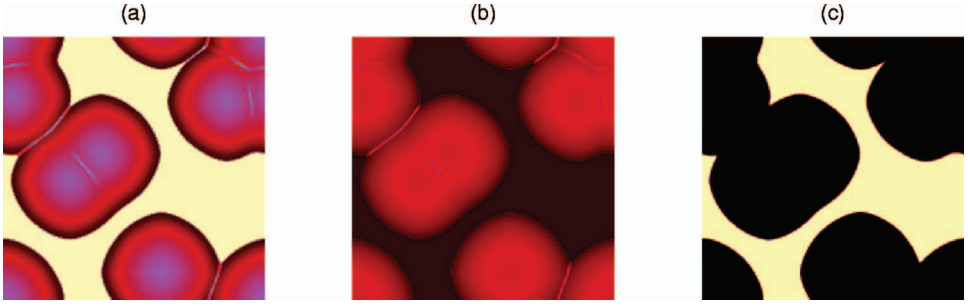

FIG. 12. (Color) Space-space diagrams (600×600 μm$^2=3.6\times10^5$ μm^2) showing the variation in the (a) 1×1, (b) total CO, and (c) total oxygen coverages during the passage of a simple CO front in a 2D simulation. Colorscale is the same as for Fig. 5. The reactant partial pressures are $p_{O_2}=6.0\times10^{-5}$ mbar and $p_{CO}=1.0\times10^{-6}$ mbar, and the temperature is 480 K. The elapsed time, t, since the beginning of the simulation is 500 s. The bulk initial conditions are ($\theta_{1\times1}$, $\theta_O^{1\times1}$, $\theta_{CO}^{1\times1}$, θ_{CO}^{hex})=(0.735, 2.98×10^{-4}, 0.402, 3.54×10^{-2}), and there are 2×2 cell defects where ($\theta_O^{1\times1}$, $\theta_{CO}^{1\times1}$, θ_{CO}^{hex})=(1.10×10^{-3}, 0.341, 1.98×10^{-2}), and $\theta_{1\times1}$=0.134, 0.234, 0.334, 0.134, 0.234, and 0.334 with bottom left corners at (1,1), (75,111), (51,91), (121,21), (171,151), and (7,155), respectively, on a 200×200 grid. (See also Fig. 2 of Ref. 15.)

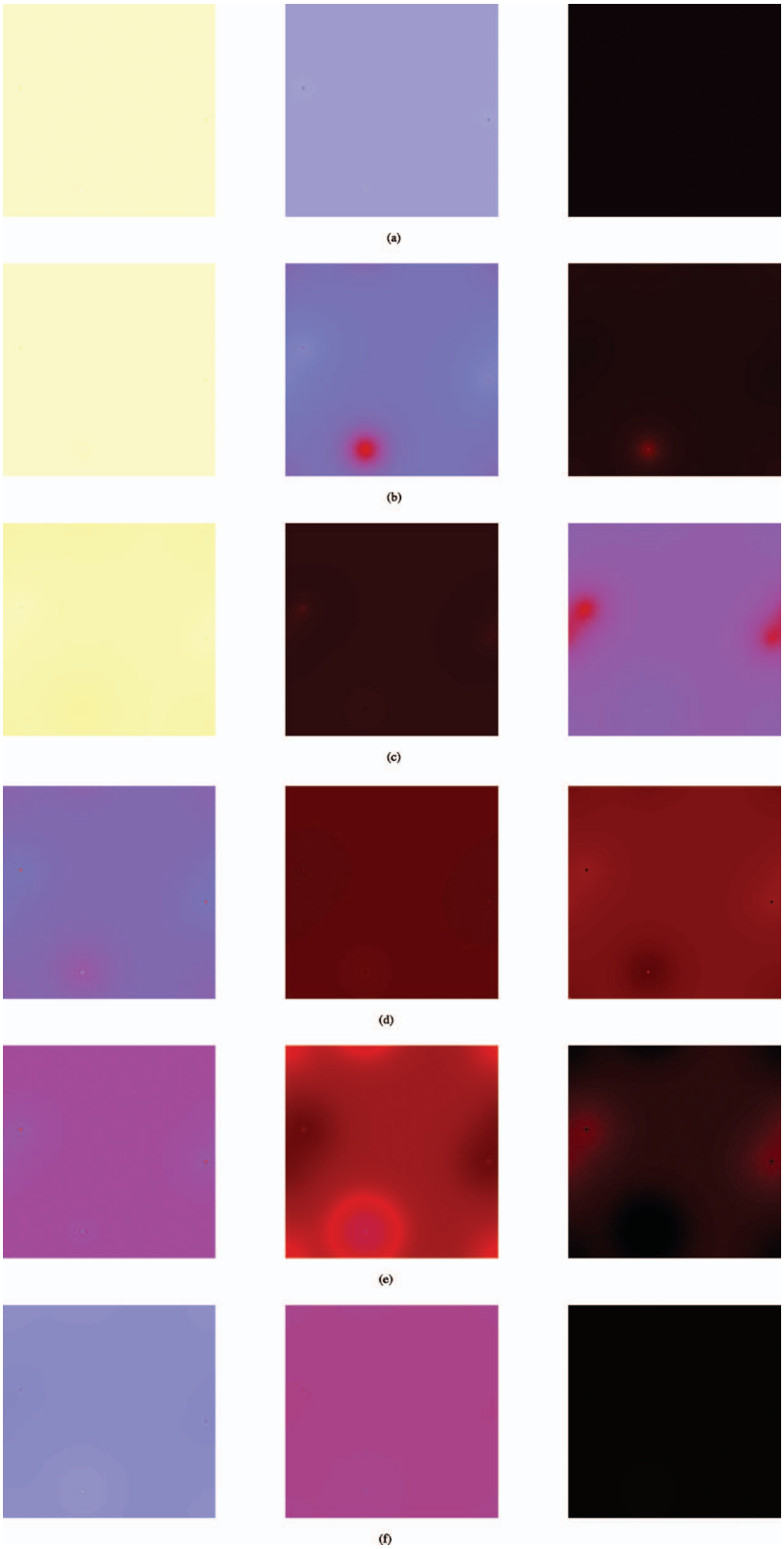

FIG. 13. (Color) Time sequence of space-space diagrams for a simulation with $p_{O_2}=7.0\times10^{-5}$ mbar and $p_{CO}=3.0\times10^{-6}$ mbar, showing the structure of the oxygen-CO reaction wave fronts. The lefthand, center, and righthand plots show the 1×1, total CO, and total oxygen coverages, respectively. Colorscale is the same as for Fig. 5. The rows give snapshots at times t=(a) 79, (b) 86, (c) 87, (d) 94, (e) 95, and (f) 100 s. The bulk initial conditions are $(\theta_{1\times1}, \theta_O^{1\times1}, \theta_{CO}^{1\times1}, \theta_{CO}^{hex})=(0.735\ 2.98\times10^{-4}, 0.402, 3.54\times10^{-2})$, and there are single cell defects, where $(\theta_O^{1\times1}, \theta_{CO}^{1\times1}, \theta_{CO}^{hex})=(1.10\times10^{-3}, 0.341, 1.98\times10^{-2})$, and $\theta_{1\times1}=0.834$, 0.134, 0.934, and 0.234 in cells (1,1), (9,61), (38,13), and (96,46), respectively, on a 100×100 grid.

integration times $t=79$ and 100 s for $p_{O_2}=7.0\times10^{-5}$ mbar and $p_{CO}=3.0\times10^{-6}$ mbar. The reactant partial pressures and the temperature are the same as for the 1D simulation shown in Fig. 10, and as expected, the qualitative behavior is the 2D analog of that seen in the 1D case. Roughly circular reaction waves propagate outwards from the defects, while the surface undergoes regular oscillations. Much less than one period of oscillation is shown in the figure so that we can capture the passing of the successive CO and oxygen fronts. Initially (time $t=79$ s), the surface is in a high 1×1 state with relatively high total CO coverage and very low levels of adsorbed oxygen. At time $t=86$ s (second row in Fig. 13), an oxygen wave spreads out from the defect in cell (38,13) and CO coverage drops ahead of it. By $t=87$ s, a moderate concentration of adsorbed oxygen covers nearly all the surface, and the fraction of 1×1 phase starts to drop. The coverages

of 1×1 phase and oxygen both now drop over the entire surface, and total CO coverage remains low ($t=94$ s, fourth row of Fig. 13) until $t=95$ s when a low-amplitude CO front spreads out from the defect at position (38,13). By $t=100$ s, levels of CO and 1×1 are recovering. Although phase change occurs during the passage of the combined oxygen-CO front, it is not as dramatic and sharply defined spatially as in the case of the simple CO front.

It was difficult to make an accurate estimate of the oxygen-CO front speeds owing to the presence of the background oscillations and the complexity of the patterns produced by the interacting defects. Comparing oxygen coverage patterns at times $t=86$ and 87 s, the initial oxygen wave appears to be traveling quite fast: between about 250 and 300 μm s^{-1}. The subsequent CO front seems to be moving more slowly, with its speed being estimated at between 10 and 20 μm s^{-1}. It is interesting to note that the oxygen wave speed is much faster than in the corresponding one-dimensional case (Fig. 10). The curvature of the two-dimensional front and the influences of other defects (which are different in the two situations) might account for this difference. It appears from Fig. 13 that the residual effect of the defects at cells (9,61) and (96,46) may also be important.

We now compare our two-dimensional simulations with experiment. There are comparatively few experimental studies showing pattern formation during CO oxidation on Pt{100}, in contrast with the case of a Pt{110} surface, where rotating spirals and pulsating target patterns, the two-dimensional equivalents of traveling waves, are commonly observed. This difference in behavior is attributed to the difference in kinetics of the phase transitions and the fact that for Pt{100}, the adsorption probability of oxygen on the hex phase is about 100 times less than that on the 1×1 phase, while for Pt{110}, the difference is only about a factor of 2.[19] Where two-dimensional patterns have been observed on Pt{100}, they are usually much more irregular than the spirals and targets typical of oscillatory systems in general.

Continuously varying spatial pattern formation has been seen on Pt{100} at temperatures of 480–500 K and partial pressures p_{O_2} in the range of $(5-9)\times10^{-5}$ mbar and p_{CO} in the range of $(5-8)\times10^{-6}$ mbar using LEED.[2] The surface was covered in irregular patches of adsorbed oxygen and CO whose arrangement changed in time through wave propagation. Typically, a CO island of a few microns across would be nucleated and then expand with constant velocity into the oxygen-covered surface. The CO island would then rapidly change to a high-oxygen state, which would finally shrink, in turn, as neighboring CO patches invaded. Oxygen waves were also seen. The CO and oxygen wave fronts moved with speeds in the range of (0.5–3) mm min^{-1} (8.3–50 μm s^{-1}).

Subsequent photoemission electron microscopy (PEEM) experiments also imaged dynamic spatiotemporal pattern formation during CO oxidation on Pt{100}. The first investigation of this type in the parameter regime for sustained oscillations[3] (380–530 K and p_{CO} and p_{O_2} up to several times 10^{-4} mbar) found rapidly changing patterns where areas of high-oxygen coverage formed spontaneously at random locations and propagated in irregular waves across the surface, finally diminishing after about 40 s. The velocity of the oxygen fronts was measured at ~100 μm s^{-1} at a surface temperature of 480 K and partial pressures $p_{O_2}=2.85\times10^{-4}$ mbar and $p_{CO}=2.0\times10^{-5}$ mbar. Less frequently observed but nevertheless present were slower moving and fairly isotropic trigger waves of oxygen islands originating from a few nucleation centers and growing in roughly circular patterns on a time scale of several minutes. The oscillations associated with these circular patterns were of large amplitude and fairly regular periodicity.

PEEM studies by Lauterbach and Rotermund[4] (also recently reviewed and summarized in Ref. 19) at temperatures between 420 and 540 K, with fixed $p_{O_2}=4\times10^{-4}$ mbar and variable CO partial pressure of a few times 10^{-5} mbar, found both CO and oxygen fronts. At $T=475$ K and $p_{CO}=1.8\times10^{-5}$ mbar, for example, a CO island nucleated on an oxygen-covered surface and spread in a fairly isotropic manner, before itself being consumed by a faster-moving oxygen front coming in from behind. In contrast, at $T=475$ K and $p_{CO}=3.6\times10^{-5}$ mbar, many smaller irregular patches could be seen. Oxygen fronts advanced into CO-covered areas, followed immediately by new CO fronts. The speeds of oxygen fronts lie in the range of 50–240 μm s^{-1}, while CO fronts were much slower at 2–26 μm s^{-1}. The difference was attributed[19] to the fact that the coverage at the reaction interface of CO fronts was low enough to initiate the 1×1 to hex phase transition, while for oxygen fronts, this was not the case.

Comparing our simulations with these experimental findings, the CO fronts in our model correspond closely to those observed in the early LEED study[2] and in the PEEM experiments of Lauterbach and Rotermund.[4] The experimental wave speeds are an order of magnitude greater than we found for our model, but in both cases, one or both of the reactant partial pressures were higher than those for which we found simple CO fronts. In agreement with Refs. 4 and 19, we find that the slow speed of propagation corresponds to the surface undergoing phase change at the front. Lauterbach and Rotermund[4] suggest that the 1×1 coverage dips at the leading edge of the front and recovers behind it. This is similar to what we see at higher p_{CO}, while for low values, the surface remains in the hex phase behind the front.

The combined oxygen-CO fronts we see somewhat resemble the patterns seen by Lauterbach and Rotermund,[4] created by consecutive waves of oxygen and CO, though the experimental pressures are an order of magnitude higher than we used in our calculations, so the results are not directly comparable. The temperature and partial pressures we chose are closest to those of the early LEED experiments,[2] where both oxygen and CO waves were observed, though at low resolution and so with less detail than in the later studies. Our simulated reaction waves travel at speeds that are in broad agreement with those seen in the experiments of Lauterbach and Rotermund, and in keeping with the argument of Lele and Lauterbach[19] for faster oxygen than CO fronts, we find that the phase change is more gradual and of lower amplitude for oxygen-CO fronts compared with the slower-moving simple CO fronts (see the 1D results in Figs. 8 and 10).

DISCUSSION

Our mesoscopic spatiotemporal model is a faithful and detailed mathematical representation of the catalytic oxidation of carbon monoxide on Pt{100} at low pressures incorporating a large amount of experimental data. It splits the (p_{O_2} and p_{CO}) parameter space, according to the type of pattern observed, into regions of very similar shape to those mapped out experimentally. Given the complexity of the detailed reaction dynamics included in the model, we were pleased by the closeness of the match. It certainly suggests that our mesoscopic modeling approach, where spatial information is determined on a scale intermediate between the microscopic spacing of the platinum atoms and the macroscopic length scale of pattern formation, captures the character of these surface patterns accurately. Compared with microscopic (lattice gas) simulations, our method is faster and requires less computational effort over larger areas of surface and so is efficient for the investigation of patterns that typically occur at scales much longer than the adsorption site spacing.

The experimental region exhibiting self-sustaining oscillations is slightly shifted toward higher p_{O_2} and p_{CO} partial pressures compared with the results of our model. The move to lower p_{O_2} in our simulations can be explained by the fact that we use the slightly higher oxygen sticking probability for freed (as opposed to free) sites over the whole 1×1 phase and by the difficulty of determining cutoffs to distinguish between stationary and oscillatory behaviors. The shift to a lower p_{CO} might be explained by the fact that p_{CO} was increased stepwise in the experiments and then was iterated about its final value, giving a lower average value over the course of the pattern evolution compared to our simulations where the target p_{CO} was fixed from the beginning. If the experimental region had been plotted using this lower average value of p_{CO}, it would be shifted toward lower values of p_{CO} and so might lie closer to the oscillatory region determined from the simulations.

The passing of successive waves of adsorbed oxygen and carbon monoxide is characteristic of the continuously varying spatial pattern formation seen in the experiment.[2–4] Our simulations reproduce this aspect of the reaction well: we see two types of traveling wave (CO and oxygen-CO) that correspond reasonably closely in terms of speed and extent of phase change to experimentally observed CO and oxygen fronts. The mesoscopic approach that we have found successful here in modeling the oxidation of CO on Pt{100} can be adapted to other surface reactions where there is spatial organization on scales that are long compared with the spacing between surface atoms.

ACKNOWLEDGMENTS

This work was supported by the Leverhulme Trust.

[1] M. Eiswirth, R. Schwanker, and G. Ertl, Z. Phys. Chem., Neue Folge **144**, 59 (1985).
[2] H. H. Rotermund, S. Jakubith, A. von Oertzen, and G. Ertl, J. Chem. Phys. **91**, 4942 (1989).
[3] H. H. Rotermund, W. Engel, M. Kordesch, and G. Ertl, Nature (London) **343**, 355 (1990).
[4] J. Lauterbach and H. H. Rotermund, Surf. Sci. **311**, 231 (1994).
[5] T. Engel and G. Ertl, J. Chem. Phys. **69**, 1267 (1978).
[6] G. Ertl, Surf. Sci. **287**, 1 (1993).
[7] P. Heilmann, K. Heinz, and K. Müller, Surf. Sci. **83**, 487 (1979).
[8] Y. T. Yeo, C. E. Wartnaby, and D. A. King, Science **268**, 1731 (1995).
[9] A. Hopkinson and D. A. King, Faraday Discuss. **96**, 255 (1993).
[10] A. Hopkinson, X.-C. Guo, J. M. Bradley, and D. A. King, J. Chem. Phys. **99**, 8262 (1993).
[11] A. Hopkinson and D. A. King, Chem. Phys. **177**, 433 (1993).
[12] D. A. King, Surf. Rev. Lett. **1**, 435 (1994).
[13] P. A. Thiel, R. J. Behm, P. R. Norton, and G. Ertl, J. Chem. Phys. **78**, 7448 (1983).
[14] A. Hopkinson, J. M. Bradley, X.-C. Guo, and D. A. King, Phys. Rev. Lett. **71**, 1597 (1993).
[15] R. B. Hoyle, A. T. Anghel, M. R. E. Proctor, and D. A. King, Phys. Rev. Lett. **98**, 226102 (2007).
[16] G. Ertl, P. R. Norton, and J. Rüstig, Phys. Rev. Lett. **49**, 177 (1982).
[17] M. P. Cox, G. Ertl, and R. Imbihl, Phys. Rev. Lett. **54**, 1725 (1985).
[18] R. Imbihl, M. P. Cox, and G. Ertl, J. Chem. Phys. **84**, 3519 (1986).
[19] T. Lele and J. Lauterbach, Chaos **12**, 164 (2002).
[20] M. A. Barteau, E. I. Ko, and R. J. Madix, Surf. Sci. **102**, 99 (1981).
[21] M. Gruyters, T. Ali, and D. A. King, Chem. Phys. Lett. **232**, 1 (1995).
[22] M. Gruyters, T. Ali, and D. A. King, J. Phys. Chem. **100**, 14417 (1996).
[23] A. Borg, A.-M. Hilmen, and E. Bergene, Surf. Sci. **306**, 10 (1994).
[24] I. M. Irurzun, R. B. Hoyle, M. R. E. Proctor, and D. A. King, Chem. Phys. Lett. **377**, 269 (2003).
[25] N. McMillan, T. Lele, C. Snively, and J. Lauterbach, Catal. Today **105**, 244 (2005).
[26] J. Lauterbach and H. H. Rotermund, Catal. Lett. **27**, 27 (1994).
[27] S. Jakubith, H. H. Rotermund, W. Engel, A. von Oertzen, and G. Ertl, Phys. Rev. Lett. **65**, 3013 (1990).
[28] P. van Beurden, B. S. Bunnik, G. J. Kramer, and A. Borg, Phys. Rev. Lett. **90**, 066106 (2003).